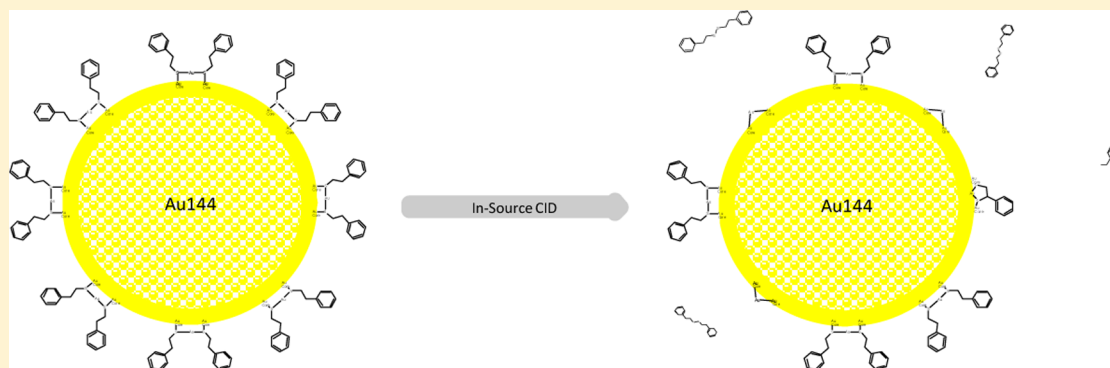# Collision-Induced Dissociation of Monolayer Protected Clusters Au$_{144}$ and Au$_{130}$ in an Electrospray Time-of-Flight Mass Spectrometer

David M. Black,[†] Nabraj Bhattarai,[‡] Robert L. Whetten,*,[‡] and Stephan B. H. Bach*,[†]

[†]Department of Chemistry, University of Texas at San Antonio, One UTSA Circle, San Antonio, Texas 78249, United States
[‡]Department of Physics and Astronomy, University of Texas at San Antonio, One UTSA Circle, San Antonio, Texas 78249, United States

S *Supporting Information*

ABSTRACT: Gas-phase reactions of larger gold clusters are poorly known because generation of the intact parent species for mass spectrometric analysis remains quite challenging. Herein we report in-source collision-induced dissociation (CID) results for the monolayer protected clusters (MPCs) Au$_{144}$(SR)$_{60}$ and Au$_{130}$(SR)$_{50}$, where R- = PhCH$_2$CH$_2$-, in a Bruker micrOTOF time-of-flight mass spectrometer. A sample mixture of the two clusters was introduced into the mass spectrometer by positive mode electrospray ionization. Standard source conditions were used to acquire a reference mass spectrum, exhibiting negligible fragmentation, and then the capillary-skimmer potential difference was increased to induce in-source CID within this low-pressure region ($\sim$4 mbar). Remarkably, distinctive fragmentation patterns are observed for each MPC[3+] parent ion. An assignment of all the major dissociation products (ions and neutrals) is deduced and interpreted by using the distinguishing characteristics in the standard structure-models for the respective MPCs. Also, we propose a ring-forming elimination mechanism to explain R-H neutral loss, as separate from the channels leading to RS-SR or (AuSR)$_4$ neutrals.

INTRODUCTION

Nanomaterial and nanoparticle science is currently a topic of enthusiastic research in the fields of biomedicine,[1−3] analytical chemistry,[4−7] physical chemistry,[8−10] and materials science.[11−13] A specific subgroup of these materials, monolayer-protected clusters (MPCs),[14,15] which are generally less than 5 nm in core diameter, represent one frontier of nanoparticle research. MPCs comprise a metal core surrounded by a layer of small ligands, typically organic thiolates. The core atoms often include one or more of the noble-metal elements.[14,15] Composition and number of the atoms in the core largely determine the electro-optical properties of the nanoparticle, which have been shown to be molecular in nature.[14−16] The thiolate ligands, denoted by RS-, which surround the core, may influence the optical properties of the MPC. However, the most significant role played by these ligands is a chemical one. Ligands can be selected to produce MPCs with surfaces of varying polarity, conferring solubility under a range of solvent conditions. For example, metal clusters protected by a monolayer of phenylethanethiolate ligands (denoted by peth;

or RS- = PhCH$_2$CH$_2$S-) are highly soluble in toluene, a nonpolar solvent; whereas ligand R-groups containing acid or base functionalities are soluble in polar solvents, including water and methanol, within the appropriate pH range. Accounts over the past decade have demonstrated that selected MPCs of various sizes can be synthesized reproducibly, and with good yield, to produce homogeneous products.[16−20] The smaller nanoparticles with core diameters <2 nm, containing fewer than $\sim$200 metal atoms, are of special interest because of a potential applicability for medicines and therapeutic delivery.[21−23] Conjugation of biologically active small molecules, peptides, oligonucleotides, etc. to nanoparticles is thought likely to improve drug metabolism and pharmacokinetic (DMPK) profiles, such that an increased drug efficacy may be observed.[22,24]

In this article, we report and discuss what we believe are the first accounts of collision-induced dissociation (CID) of $Au_{144}(SR)_{60}$ and $Au_{130}(SR)_{50}$ MPCs. These are not only among the best studied of the compositionally defined larger MPCs but also lie in the critical transition zone where metal-cluster properties become much more similar to the extended self-assembled monolayers (SAMs) formed on planar gold electrodes.[15] The larger cluster is understood to have a core structure based on the icosahedral Pd_{145} crystal structure of Tran et al.[25,26] The definite composition (144 Au atoms and 60 thiolate ligands) was suggested based on ESI-MS in 2008 by Chaki et al.,[27] followed closely by more definitive reports of Fields-Zinna et al.[28] as well as Qian and Jin.[29] The first complete structure model consistent with this composition was also reported in 2009;[30] this structure was refined[31] in 2013 to ensure *I*-symmetry compliance, in agreement with the NMR measurements[32] demonstrating the 60-fold symmetry equivalence of the ligand R-groups. For further discussion of this symmetry type, see ref 33. The smaller (130,50) MPC was first determined in 2012 by Negishi et al.[34] and has been investigated more recently in great detail by Jupally et al.[35] The structure model proposed in the former report has been explored by high-level (DFT) calculations of Tlahuice et al.[36] We emphasize that only the Pd_{145} crystal structure has been determined unambiguously; the others should be regarded as the standard or conventional structure models, at the present.

At present, gas-phase characterization performed on such larger MPCs has been restricted to "full scan" mass spectrometry by matrix assisted laser desorption ionization (MALDI) and/or electrospray ionization (ESI) mass spectrometry, wherein the aim is to produce intact parent ions and fragmentation-free spectra. Peaks attributable to residual fragmentation are nonetheless frequently identified and discussed in terms of the energetic stability of the inferred neutral and charged products. Clearly, a more reliable approach is to induce fragmentation in gas-phase parent ions that are first introduced intact into the vapor phase and thermalized by ambient inert gas, prior to inducing dissociation by energetic collisions. The method of in-source CID provides an efficient nonmass-selective means of inducing fragmentation.[37−44] Source voltages are configured to accelerate the ions as they pass through a transitional pressure region of the mass spectrometer held at the low millibar range (∼4 mbar). Under these conditions, numerous collisions between the accelerated ions and the background gas molecules may activate the ions, resulting in fragmentation. The patterns of fragmentation observed with in-source CID are similar to what is observed by tandem mass spectrometry in collision cells of triple quadrupole and quadrupole time-of-flight instruments.[45−48] Although tandem mass spectrometry is not yet a routine part of novel nanoparticle characterization, recent reports have demonstrated the utility of the gas-phase collisionally activated dissociation chemistry of smaller MPCs such as $Au_{25}(SR)_{18}^{[1-]}$.[49−51] Ion-mobility mass spectrometry has also been reported.[52−54] In this report, we demonstrate that CID-type analysis can be applied effectively to the considerably larger clusters of great current interest.

■ EXPERIMENTAL METHODS

Cluster Synthesis. The synthesis of $Au_{144}(SR)_{60}$ nanoclusters was carried out by using modified Brust's methods reported in the literature.[31] Briefly, the pure $Au_{144}(SR)_{60}$ nanocluster as well as the byproduct Au_{130} nanocluster were obtained in two steps with a Au:SR ratio of 1:3. In the first step, polydispersed nanoclusters were obtained, and allowed to etch (aerobic heating at 80 °C in excess thiolate ligands), converting the less stable into oxidation resistant form purely monodispersed Au_{144} nanoclusters. The properties of the pure Au_{130} nanoclusters are described in refs 34 and 35.

In the first step, tetractylammonium bromide (TOAB, 0.052 M, 10 mL toluene) was mixed with $HAuCl_4 \cdot 3H_2O$ (0.09 M, 5 mL H_2O) in a 25-mL round-bottomed flask and vigorously stirred for 1 h until the phase transfer of Au(III) from the aqueous phase changed to the Au(III) toluene phase. The clear phase between toluene (deep red) and aqueous (colorless) indicated the complete phase transfer. The aqueous part was removed and the deep red toluene solution was cooled at 0 °C for 30 min. Then 186 μL of $PhCH_2CH_2SH$ was added to the stirred solution of Au(III) and with continued stirring for 1 h. The color changed from deep red to yellow and finally colorless. The $PhCH_2CH_2SH$ capped Au(III) particles were reduced by adding $NaBH_4$ (0.171 g, 5 mL in water) at once. The quick addition of $NaBH_4$ to the Au(III) solution changed the color to black indicating the formation of the nanoclusters. The reaction was allowed to proceed for 24 h so that all the excess $NaBH_4$ decomposed. The aqueous phase was removed and the black residue with toluene was dried, using a rotary evaporator. The sample obtained after rotovapping was washed with ethanol and allowed to precipitate in a refrigerator. The washed precipitate was dried in the atmosphere and ready for characterization and for etching in the second step.

In the second step, 0.03 g of the sample obtained from the first step was dissolved in 1.5 mL of toluene in a 5 mL vial. One milliliter of $PhCH_2CH_2SH$ was added and the solution was continuously stirred for 24 h at 80 °C. Then the solution was transferred to a new 25-mL vial, excess methanol was added to the mixture, and the particles were allowed to precipitate in a refrigerator for 15 h. The methanol was removed and the precipitate was dissolved in CH_2Cl_2 (DCM). Only the desired clusters Au_{144} and Au_{130} will be soluble in CH_2Cl_2 (brown color) thus separating it from the insoluble byproduct. The solution was further recrystallized for electron microscopy and electrospray characterization.

Mass Spectrometry. All mass spectrometry data were collected on a Bruker micrOTOF time-of-flight mass spectrometer with electrospray ionization in the positive ion mode. The $Au_{144}(SR)_{60}/Au_{130}(SR)_{50}$ mixture was dissolved in dry toluene at a concentration of approximately 1−2 mg/mL. Sample was introduced to the source of the mass spectrometer by direct infusion with 5 μL loop injections. Methanol was used as the mobile phase to push the injected sample into the electrospray source. A flow rate of 15 μL/min was chosen for best overall signal quality. Source parameters were as follows: capillary entrance voltage = −4500 V, end plate offset = −500 V, nebulizer pressure (N_2) = 45 psi, dry gas (N_2) = 5.0 L/min, dry gas temperature =60 °C. Transfer lens parameters were as follows: capillary exit = 200.0 V, skimmer 1 = 80.0 V, hexapole DC 25.0 V, hexapole rf = 800 V_{o-p}, skimmer 2 = 28.1 V. Lens 1 transfer and lens 1 prepulse storage times were 214 and 35 μs, respectively. The multichannel plate detector (MCP) voltage was increased from 2100 V, which is used for small molecule work, up to 2300 V to provide better signal strength and good signal-to-noise ratios for work with nanoparticles. Mass spectra were collected over a 15−20 s time window (5 at 15 μL per min) and averaged.

■ RESULTS AND DISCUSSION

A typical mass spectrum of a mixture of $Au_{144}(SR)_{60}$ and $Au_{130}(SR)_{50}$ is shown in Figure 1. The mass spectrum spans $m/$
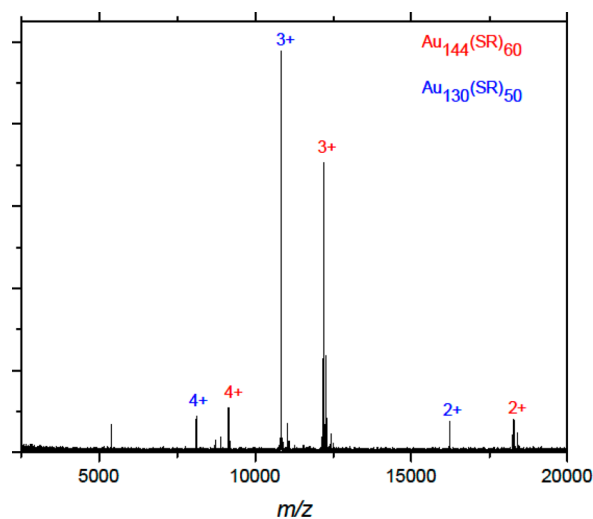
Figure 1. Positive electrospray ionization mass spectrum of a mixture of $Au_{144}(SR)_{60}$ and $Au_{130}(SR)_{50}$.

Figure 2. Mass axis expanded view centered on the [3+] charge states of $Au_{144}(SR)_{60}$ and $Au_{130}(SR)_{50}$ showing the fragment ion series formed by in-source CID.

z 2 500 to 20 000 revealing the [2+] to [4+] charge states for each of the two MPCs. Consistent with prior reports, the [3+] charge state corresponds to the ion population generating the strongest signal, and there is no evidence of the [5+] or higher charge states in the mass spectrum.[33] This is also true of spectra obtained under similar conditions on highly purified Au_{144} samples. The peak at m/z 5,388 corresponds closely to the expected m/z of $Au_{38}(SR)_{24}[2+]$, a synthetic byproduct, which does not appear to be a fragment of $Au_{144}(SR)_{60}$ or $Au_{130}(SR)_{50}$.

The in-source CID experiments were initiated by increasing the voltage differential (ΔV) between the capillary exit and skimmer. Typical focusing voltages for $Au_{144}(SR)_{60}$ and $Au_{130}(SR)_{50}$, which do not induce fragmentation, but optimize signal strength, are 200 V applied to the capillary exit lens and 80 V applied to the skimmer (ΔV = 120 V). In-source CID can be initiated by increasing this voltage differential. The mass spectra shown in Figures 2 through 4 were acquired by applying the maximum allowable potential of 400 V to the capillary exit lens and 50 V to the skimmer (ΔV = 350 V). Further increasing ΔV by lowering the skimmer potential below 50 V is impractical because of the reduced ion transmission.

The collisional characteristics of this region may be defined as follows. The nitrogen pressure in this region of the instrument is controlled, but an accurate determination of the number of ion-neutral collisions is difficult to make because of a weak free-jet expansion that ions and neutrals experience as they exit the near ambient pressure conditions of the capillary into the lower pressure region between capillary and skimmer. At best, an upper bound to the total number of ion-neutral collisions can be calculated from the mean free path of the MPCs (∼0.001 mm) at the pressure (4 mbar) of the background (nitrogen) gas, and the capillary to skimmer distance (∼3 mm). This indicates an upper bound of ∼3000 collisions; however, the actual number of collisions may be significantly lower due to the effect of the free-jet expansion.
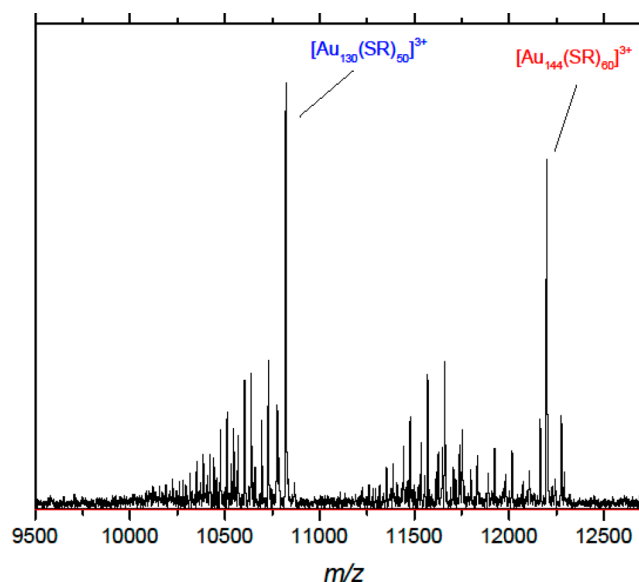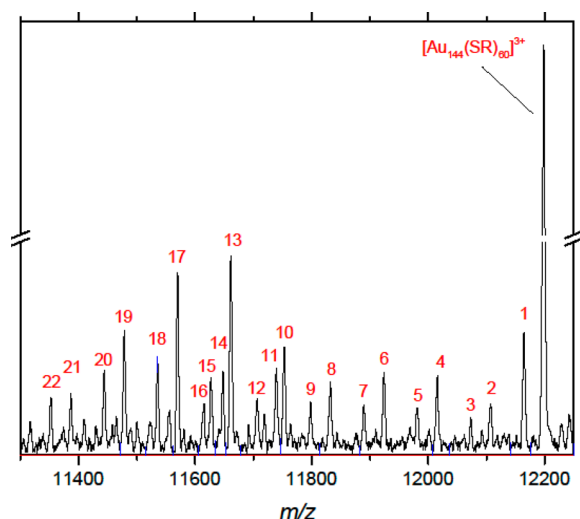
Clear differences in the extent of fragmentation were observed between the different charge states for each of the two MPCs. Minimal fragmentation (i.e., fragmentation efficiencies less than 10%) is observed for the singly charged and doubly charged ion populations of either nanoparticle, whereas the triply charged species for both $Au_{144}(SR)_{60}$ and $Au_{130}(SR)_{50}$ form more than 20 distinct fragment ions (fragmentation efficiencies of 80% and 76%, respectively). No related fragments are identified in the mass spectrum for the quadruply charged state. This may be attributed partly to the relatively low signal strength of the quadruply charged parent ions. Also, the quadruply charged ion populations may fragment to a greater extent than the triply charged populations do, producing a greater number of unique fragment ion structures, and, on average, lower signal strength for any given fragment. This "spreading" of ion current, from one ion population to many, may also be a factor in there being poor signal for any related fragment ions. Under similar conditions, the electrosprayed $Au_{25}(peth)_{18}[+]$ cluster dissociated to a large extent (>50%) to give a pattern of fragment ions in agreement with that known previously.[42]

Differences in fragmentation behavior among the different charge states for a given compound have been reported in studies of peptides, proteins, and oligonucleotides.[55−57] As is the case with biomolecules, MPC charge states likely show differences in fragmentation due to a combination of factors relating to gas-phase ion stability, ion structure, and the effect of charge state on the center-of-mass collision energy (E_{COM}). Although it is not clear whether the gas-phase structures of the MPCs differ as a function of charge state, higher charge states are expected to be less stable in the gas phase due to the destabilizing effect of Coulombic repulsion. Additionally, ions with higher charge states are accelerated to higher velocities when traveling down the voltage gradient (capillary skimmer). The translational energy gained is directly proportional to the charge state (z), so proportionately greater internal energy is imparted into the ions with each collision event for the higher charge states.
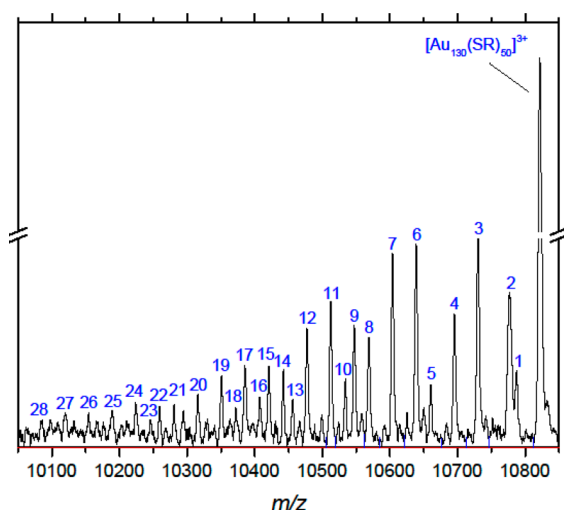
In-source CID is also capable of producing characteristic patterns of dissociation specific to each larger MPC, at the same charge state. Figure 2 shows a mass axis zoom of the [3+] charge states of both $Au_{144}(SR)_{60}$ and $Au_{130}(SR)_{50}$ with in-source CID conditions applied. Although both MPCs are comprised of the same core element and protecting organic ligands and share related structural elements, each dissociates to form a unique pattern of fragment ions and neutral losses. Under the most energetic conditions used herein for in-source CID, both $Au_{144}(SR)_{60}$ and $Au_{130}(SR)_{50}$ lose over 20 ligands and partial ligands. Due to the limits of the mass resolution of the instrument, we cannot determine the charge state of the fragment ions based on the stable isotope spacing. However, reasoning by proximity to the respective parent ions, each of the triply charged ion populations appears to lose multiple ligands and partial ligands while maintaining the charge state of the precursor ion. Accordingly, the mass spectral interpretation and fragment ion assignments in this paper are made based on that assumption. $Au_{144}(SR)_{60}$ loses a series of ligands such that fragment ions span m/z 11 300 up to the mass-to-charge of the precursor at approximately m/z 12 198. $Au_{130}(SR)_{50}$ exhibits a similar trend of fragmentation forming fragment ions spanning m/z 10 100 up to the mass-to-charge of the precursor at approximately m/z 10 822, or up to 7% of total mass. However, the pattern of neutral losses is significantly different. This clearly suggests a utility for in-source CID and tandem mass spectrometric structural characterization of MPCs and their conjugated analogues.

Further mass-axis expansions centered on the [3+] charge states of $Au_{144}(SR)_{60}$ and $Au_{130}(SR)_{50}$ and associated fragment ions are shown in Figures 3 and 4, respectively. The

Figure 4. Mass axis expanded view of the [3+] charge state of $Au_{130}(SR)_{50}$ and associated fragment ions. Numbered fragment ions are tentatively identified in Table 2.

Figure 3. Mass axis expanded view of the [3+] charge state of $Au_{144}(SR)_{60}$ and associated fragment ions. Numbered fragment ions are tentatively identified in Table 1.

corresponding fragment ion identifications are listed in Tables 1 and 2. Careful examination of this region of the mass spectrum reveals distinct patterns of losses for each of the two MPCs. Both the $Au_{144}(SR)_{60}$ and $Au_{130}(SR)_{50}$ precursors appear to lose predominantly the same neutral molecules, but exhibit different patterns with respect to the order of the loses (i.e., consecutive fragmentation). For each of the MPCs, preferred neutral losses included a dimer of the thiolate ligand, phenylethanethiolate, denoted by $(SR)_2$, in Tables 1 and 2. In

all but one case, observed in the in-source CID mass spectrum of $Au_{130}(SR)_{50}$, the loss of the thiolate ligands occurred in pairs. The structure of this neutral product may in fact be a disulfide (RS-SR) formed from a rearrangement elimination reaction involving two thiolate ligands. This type of decomposition is energetically preferred to the loss of two individual ligands.

Generally, rearrangement reactions are observed at lower activation energies (i.e., ion kinetic energy less than 100 eV). However, due to a confluence of multiple factors (i.e., MPC size, number of collisions, as well as the rates of MPC fragmentation and radiative cooling), it is likely that all of the MPC fragment ions observed are formed as a result of internal energy gains on par with what would be generally thought of as being consistent with low-energy activation. Perhaps the most significant of these factors is the large disparity in mass between the MPCs and the nitrogen source gas molecules. For example, when a 350 V in-source CID energy is applied (E_{lab}), the maximum possible increase in internal energy *per collision* (E_{com}) for an ion population of 36 595 Da is no more than ~0.27, ~0.54, ~0.80, and ~1.07 eV for the [1+], [2+], [3+], and [4+] charge states, respectively.

Partial ligand loss, represented by RH in Tables 1 and 2, was also noted to occur as part of the regular pattern of neutral losses. In this case, the hydrocarbon portion of the thiolate ligand was lost such that cleavage occurred at the sulfur—carbon bond. Again, because resolution of the various stable isotopes for these massive nanoparticles is not achieved, one cannot determine whether the neutral structure formed is that of ethylbenzene, or phenylethane (RH), a phenylethyl radical (R•), or ethenylbenzene, etc. We prefer to designate the products as even-electron neutrals (RH) because relatively low collisional activation energies (vide supra) and very large nanoparticle size (concomitant number of bonds and vibrational modes) tend to favor rearrangement reactions.

The most striking trend is the pattern that extends, almost without exception, throughout the fragment ion and neutral loss series shown in Tables 1 and 2. Each table consists of five columns showing, from left to right, a serial number, the m/z of the identified fragment ion, the molecular formula assigned to that fragment ion, and the molecular formula of the corresponding total neutral loss. The fifth column of each

Table 1. Structural Assignments for Fragment Ions and Neutral Losses of Au₁₄₄(SR)₆₀[3+]

Table 1. Structural Assignments for Fragment Ions and Neutral Losses of $Au_{144}(SR)_{60}[3+]$

| fragment ion no.	m/z	fragment ion	neutral loss	neutral loss branching series										
				1	2	3	4	5	6	7	8	9	10	11
	12198.3													
1	12163.9	$Au_{144}(SR)_{59}S$	RH	RH										
2	12107.9	$Au_{144}(SR)_{58}$	$(SR)_2$		$(SR)_2$ / RH									
3	12073.4	$Au_{144}(SR)_{57}S$	$(SR)_2RH$			$(SR)_2$ / RH								
4	12015.2	$Au_{144}(SR)_{56}$	$(SR)_4$			$(SR)_2$	$(SR)_2$ / RH							
5	11982.8	$Au_{144}(SR)_{55}S$	$(SR)_4RH$				$(SR)_2$	$(SR)_2$ / RH						
6	11924.6	$Au_{144}(SR)_{54}$	$(SR)_6$				$(SR)_2$	$(SR)_2$	$(SR)_2$ / RH					
7	11887.8	$Au_{144}(SR)_{53}S$	$(SR)_6RH$					$(SR)_2$	$(SR)_2$	$(SR)_2$ / RH				
8	11831.8	$Au_{144}(SR)_{52}$	$(SR)_8$					$(SR)_2$	$(SR)_2$	$(SR)_2$				
9	11799.5	$Au_{144}(SR)_{51}S$	$(SR)_8RH$					$(SR)_2$ / RH						
10	11754.1	$Au_{140}(SR)_{56}$	$Au_4(SR)_4$								$Au_4(SR)_4$	$Au_4(SR)_4$	$Au_4(SR)_4$	$Au_4(SR)_4$
11	11741.2	$Au_{144}(SR)_{50}$	$(SR)_{10}$						$(SR)_2$	$(SR)_2$				
12	11706.3	$Au_{144}(SR)_{49}S$	$(SR)_{10}RH$						$(SR)_2$ / RH					
13	11661.4	$Au_{140}(SR)_{54}$	$Au_4(SR)_6$								$(SR)_2$	$(SR)_2$	$(SR)_2$	$(SR)_2$
14	11648.5	$Au_{144}(SR)_{48}$	$(SR)_{12}$							$(SR)_2$				
15	11614.0	$Au_{144}(SR)_{47}S$	$(SR)_{12}RH$							$(SR)_2$ / RH				
16	11627.1	$Au_{140}(SR)_{53}S$	$Au_4(SR)_6RH$								RH	RH		
17	11568.9	$Au_{140}(SR)_{52}$	$Au_4(SR)_8$									$(SR)_2$ / RH	$(SR)_2$	$(SR)_2$
18	11536.5	$Au_{140}(SR)_{51}S$	$Au_4(SR)_8RH$									RH		
19	11480.2	$Au_{140}(SR)_{50}$	$Au_4(SR)_{10}$										$(SR)_2$	$(SR)_2$
20	11443.8	$Au_{140}(SR)_{49}S$	$Au_4(SR)_{10}RH$										RH	RH
21	11386.8	$Au_{140}(SR)_{48}$	$Au_4(SR)_{12}$											$(SR)_2$
22	11352.4	$Au_{140}(SR)_{47}S$	$Au_4(SR)_{12}RH$											RH

Table 2. Structural Assignments for Fragment Ions and Neutral Losses of $Au_{130}(SR)_{50}[3+]$

fragment ion no.	m/z	fragment ion	neutral loss	neutral loss branching series									
				1	2	3	4	5	6	7	8	9	10
	10821.9												
1	10787.2	$Au_{130}(SR)_{49}S$	RH	RH									
2	10776.6	$Au_{130}(SR)_{49}$	(SR)		(SR)								
3	10729.3	$Au_{130}(SR)_{48}$	$(SR)_2$			$(SR)_2$	$(SR)_2$	$(SR)_2$	$(SR)_2$				
4	10694.8	$Au_{130}(SR)_{47}S$	$(SR)_2RH$			RH							
5	10660.5	$Au_{130}(SR)_{46}S_2$	$(SR)_2(RH)_2$			RH							
6	10639.3	$Au_{130}(SR)_{46}$	$(SR)_4$				$(SR)_2$	$(SR)_2$	$(SR)_2$				
7	10602.9	$Au_{130}(SR)_{45}S$	$(SR)_4RH$				RH						
8	10567.8	$Au_{130}(SR)_{44}S_2$	$(SR)_4(RH)_2$				RH						
9	10547.5	$Au_{130}(SR)_{44}$	$(SR)_6$					$(SR)_2$	$(SR)_2$				
10	10533.8	$Au_{127}(SR)_{48}$	$Au_3(SR)_4$							$Au_3(SR)_2$	$Au_3(SR)_2$	$Au_3(SR)_2$	$Au_3(SR)_2$
11	10512.2	$Au_{130}(SR)_{43}S$	$(SR)_6RH$					RH					
12	10478.2	$Au_{130}(SR)_{42}S_2$	$(SR)_6(RH)_2$					RH					
13	10456.2	$Au_{130}(SR)_{42}$	$(SR)_8$						$(SR)_2$				
14	10441.9	$Au_{127}(SR)_{46}$	$Au_3(SR)_4$							$(SR)_2$	$(SR)_2$	$(SR)_2$	
15	10421.4	$Au_{130}(SR)_{41}S$	$(SR)_8RH$						RH				
16	10407.6	$Au_{127}(SR)_{45}S$	$Au_3(SR)_4RH$							RH			
17	10386.4	$Au_{130}(SR)_{40}S_2$	$(SR)_8(RH)_2$						RH				
18	10372.1	$Au_{127}(SR)_{44}S_2$	$Au_3(SR)_4(RH)_2$							RH			
19	10349.0	$Au_{127}(SR)_{44}$	$Au_3(SR)_6$								$(SR)_2$	$(SR)_2$	
20	10316.1	$Au_{130}(SR)_{43}S$	$Au_3(SR)_6RH$								RH		
21	10280.1	$Au_{127}(SR)_{42}S_2$	$Au_3(SR)_6(RH)_2$								RH		
22	10259.2	$Au_{127}(SR)_{42}$	$Au_3(SR)_8$									$(SR)_2$	
23	10245.8	$Au_{124}(SR)_{46}$	$Au_6(SR)_4$										$Au_3(SR)_2$
24	10224.1	$Au_{127}(SR)_{41}S$	$Au_3(SR)_8RH$									RH	
25	10189.1	$Au_{127}(SR)_{40}S_2$	$Au_3(SR)_8(RH)_2$									RH	
26	10153.9	$Au_{124}(SR)_{44}$	$Au_6(SR)_6$										$(SR)_2$
27	10119.8	$Au_{124}(SR)_{43}S$	$Au_6(SR)_6RH$										RH
28	10085.2	$Au_{124}(SR)_{42}S_2$	$Au_6(SR)_6(RH)_2$										RH

table has multiple subcolumns that show the various neutral loss branching series deduced from the fragmentation patterns for each MPC. Both $Au_{144}(SR)_{60}$ and $Au_{130}(SR)_{50}$ patterns may be explained by an alternating series of complete ligand (RS-SR) vs partial-ligand (R-H) neutral losses. However, the patterns for the two MPCs differ in a significant way. $Au_{144}(SR)_{60}$ follows the repeating pattern of neutral losses,

$$-(SR)_{2N}-[(SR)_{2N} + RH]-$$

whereas $Au_{130}(SR)_{50}$ follows the pattern

$$-(SR)_{2N}-[(SR)_{2N} + (RH)_2]-$$
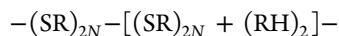
Analysis of the neutral loss branching series shows that each branching pathway terminates after loss of one RH functional group for $Au_{144}(SR)_{60}$ but two sequential losses of RH for $Au_{130}(SR)_{50}$.

This intriguing difference may be related to the specific structural characteristics of the two MPCs. Interestingly, the detailed structure models discussed in refs 30−36 agree that the ligand bridges, or staples, present in the protecting monolayer for the two nanoparticles are not all identical. The $Au_{144}(SR)_{60}$ structure features only the (30) short three-atom containing staples, (−S−Au−S−) while the $Au_{130}(SR)_{50}$ structure was reported to contain both short (20) and long (5) five-atom containing staples (−S−Au−S−Au−S−).[36] This variation in staple length may be the predominant factor leading to the differing fragmentation patterns observed between the two MPCs. Accordingly, we searched for a relatively simple ring-forming rearrangement reaction that may explain this fragmentation behavior.

Schemes 1 and 2 show tentative fragment ion structures that are consistent with the branching patterns noted above. For

Scheme 1. Loss of RH from the Short Staple Motif To Form a Monocyclic Structure
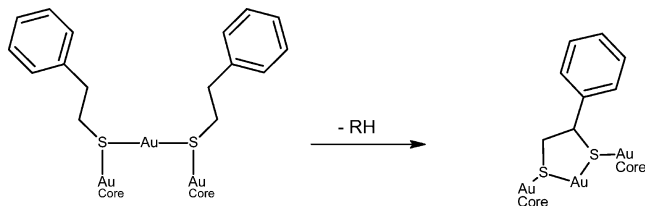
both staple configurations, an ethylbenzene neutral molecule is lost, via a rearrangement elimination reaction. As part of the pattern of consecutive loses described above, each staple of $Au_{144}(SR)_{60}$ is capable of losing only one RH moiety while the $Au_{130}(SR)_{50}$ structure-model should be capable of losing one or two of these functionalities. Because there are two and three thiolate ligands on the short and long staples, respectively, it seems likely that a rearrangement reaction is occurring such that a stable configuration is formed that prevents the loss of the last RH moiety from each of the two staple types. It may be that due to the steric flexibility of the phenylethanethiol and ligand staple motif, considering the various rotational and vibrational modes, the sulfur of one ligand is able to come into close enough proximity with the β-carbon of the neighboring ligand to form a five-member transition state. This may then allow for one of the hydrogens bound to the β-carbon to be transferred to the neighboring ethylbenzene, initiating elimination of that ethylbenzene and concomitant formation of a sulfur−carbon bond. Short staples are able to lose one neutral

Scheme 2. Loss of One, and Two, RH Neutrals from the Long Staple Motif To Form Monocyclic and [2.2.1] Bicyclic Structures
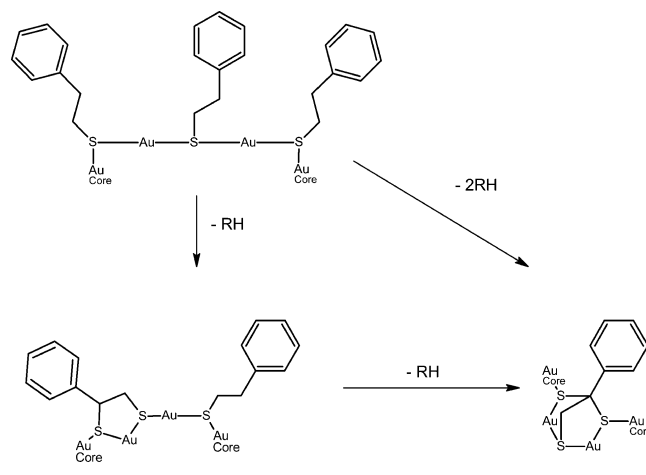
hydrocarbon in this way to form a stable five-member ring. Long staples are capable of losing two neutral hydrocarbons, in this same manner, which results in the formation a five- and six-member [2.2.1] bicyclic structure.

Besides these organic-group rearrangements, neutral losses containing gold atoms were also observed for both nanoparticles. These losses are denoted in Tables 1 and 2 in bold text. Based on what was observed in this study, these types of losses appear to be specific to the identity and structure type of the precursor. This is in contrast to the ligand-related losses which are consistent with the ligand identity, but do not alone provide sufficient structurally diagnostic information for the purpose of differentiating nanoparticle core size. $Au_{144}(SR)_{60}$ fragments to form a second series of consecutive neutral losses beginning with $Au_4(SR)_4$. The formation of $Au_4(SR)_4$ fragment ions and neutral losses by CID of smaller MPCs has been observed and reported previously by earlier groups.[49,54] $Au_{130}(SR)_{50}$ loses a different gold-containing neutral loss series, based on $Au_3(SR)_2$. The same branching pattern of thiol and hydrocarbon losses discussed above was observed to occur with the gold atom containing neutral losses.

■ CONCLUSIONS

In summary, we have shown new results that demonstrate the applicability of in-source CID mass spectrometry for gas-phase characterization of gold MPCs up to mass 36 kDa. In-source dissociation was initiated by accelerating MPC parent ions between the capillary exit and skimmer region of the mass spectrometer, using the maximum practical voltage gradient. Greater fragmentation efficiencies were observed for the higher charge states of each of the two MPCs, $Au_{144}(SR)_{60}$ and $Au_{130}(SR)_{50}$. Fragmentation patterns for the two MPCs were notably distinct and are consistent with the accepted differences in MPC structure types. Consecutive fragmentation patterns and neutral losses, characteristic of each MPC, were identified. Both MPCs fragmented to lose the R-group hydrocarbon portion of the thiolate ligand, as RH, as well as the intact thiolate itself, as RS-SR. In all but one case, the thiolate ligand appeared to be lost in pairs, $(SR)_2$. Neutral losses containing gold atoms were also observed. The composition of these types of losses varied and appeared to be specific to the originating MPC core type.

Future studies will be aimed at investigating methods for improving the fragmentation efficiencies of the lower MPC charge states as well as the characterization of MPCs with different protecting ligand structures. Straightforward extensions of this work will allow comparative investigations of the CID patterns of many other protected metallic clusters that previously have been analyzed by ESI-MS without any gas-phase characterization.

■ ASSOCIATED CONTENT

Ⓢ Supporting Information

Positive electrospray ionization mass spectrum of $Au_{25}(SR)_{18}$ with and without in-source CID conditions applied to induce fragmentation. This material is available free of charge via the Internet at http://pubs.acs.org.

■ AUTHOR INFORMATION

Corresponding Authors
* E-mail: robert.whetten@utsa.edu (R.L.W.).
* E-mail: stephan.bach@utsa.edu (S.B.H.B.).

Notes
The authors declare no competing financial interests.

■ ACKNOWLEDGMENTS

■ REFERENCES

(1) Huang, X. H.; Peng, X. H.; Wang, Y. Q.; Wang, Y. X.; Shin, D. M.; El-Sayed, M. A.; Nie, S. M. A Reexamination of Active and Passive Tumor Targeting by Using Rod-Shaped Gold Nanocrystals and Covalently Conjugated Peptide Ligands. *ACS Nano* **2010**, *4*, 5887−5896.

(2) Elsaesser, A.; Taylor, A.; de Yanes, G. S.; McKerr, G.; Kim, E. M.; O'Hare, E.; Howard, C. V. Quantification of Nanoparticle Uptake by Cells Using Microscopical and Analytical Techniques. *Nanomedicine* **2010**, *5*, 1447−1457.

(3) Hinterwirth, H.; Lindner, W.; Lammerhofer, M. Bioconjugation of Trypsin onto Gold Nanoparticles: Effect of Surface Chemistry on Bioactivity. *Anal. Chim. Acta* **2012**, *733*, 90−97.

(4) Liu, X.; Li, W. J.; Li, L.; Yang, Y.; Mao, L. G.; Peng, Z. A Label-Free Electrochemical Immunosensor Based on Gold Nanoparticles for Direct Detection of Atrazine. *Sens. Actuators, B* **2014**, *191*, 408−414.

(5) Crosby, J. S.; James, J. Z.; Lucas, D.; Koshland, C. P. Determination of Total Mercury Concentration in Aqueous Samples with Gold Nanoparticles. *Anal. Methods* **2014**, *6*, 1254−1260.

(6) Zamborini, F. P.; Bao, L. L.; Dasari, R. Nanoparticles in Measurement Science. *Anal. Chem.* **2012**, *84*, 541−576.

(7) Ya, Y.; Mo, L. X.; Wang, T. S.; Fan, Y. G.; Liao, J.; Chen, Z. L.; Manoj, K. S.; Fang, F. X.; Li, C. Y.; Liang, J. Highly Sensitive Determination of Capsaicin Using a Carbon Paste Electrode Modified with Amino-Functionalized Mesoporous Silica. *Colloids Surf., B* **2012**, *95*, 90−95.

(8) Zhang, Z. J.; Rong, F.; Xie, Y. B.; Wang, Y.; Yang, H. Y.; Fu, D. G. Controllable Assembly of Dimers and Trimers of Gold Nanoparticle Bridged by Tris(2-Aminoethyl)Amine. *J. Nanosci. Nanotechnol.* **2011**, *11*, 2163−2167.

(9) Guillermier, C.; Della-Negra, S.; Schweikert, E. A.; Dunlop, A.; Rizza, G. Emission of Molecular Fragments Synthesized in Hyper-velocity Nanoparticle Impacts. *Int. J. Mass Spectrom.* **2008**, *275*, 86−90.

(10) Qian, H. F.; Zhu, Y.; Jin, R. C. Atomically Precise Gold Nanocrystal Molecules with Surface Plasmon Resonance. *Proc. Natl. Acad. Sci. U.S.A.* **2012**, *109*, 696−700.

(11) Nimmala, P. R.; Yoon, B.; Whetten, R. L.; Landman, U.; Dass, A. $Au_{(67)}(SR)_{(35)}$ Nanomolecules: Characteristic Size-Specific Optical, Electrochemical, Structural Properties and First-Principles Theoretical Analysis. *J. Phys. Chem. A* **2013**, *117*, 504−517.

(12) Jiang, D. E.; Nobusada, K.; Luo, W.; Whetten, R. L. Thiolated Gold Nanowires: Metallic Versus Semiconducting. *ACS Nano* **2009**, *3*, 2351−2357.

(13) Kim, B. H.; Hackett, M. J.; Park, J.; Hyeon, T. Synthesis, Characterization, and Application of Ultrasmall Nanoparticles. *Chem. Mater.* **2014**, *26*, 59−71.

(14) Qian, H. F.; Zhu, M. Z.; Wu, Z. K.; Jin, R. C. Quantum Sized Gold Nanoclusters with Atomic Precision. *Acc. Chem. Res.* **2012**, *45*, 1470−1479.

(15) Maity, P.; Xie, S.; Yamauchi, M.; Tsukuda, T. Stabilized Gold Clusters: From Isolation toward Controlled Synthesis. *Nanoscale* **2012**, *4*, 4027−4037.

(16) Schaaff, T. G.; Shafigullin, M. N.; Khoury, J. T.; Vezmar, I.; Whetten, R. L.; Cullen, W. G.; First, P. N.; GutierrezWing, C.; Ascensio, J.; JoseYacaman, M. J. Isolation of Smaller Nanocrystal Au Molecules: Robust Quantum Effects in Optical Spectra. *J. Phys. Chem. B* **1997**, *101*, 7885−7891.

(17) Parker, J. F.; Weaver, J. E. F.; McCallum, F.; Fields-Zinna, C. A.; Murray, R. W. Synthesis of Monodisperse $[Oct_4N^+][Au_{25}(SR)_{18}{}^-]$ Nanoparticles, with Some Mechanistic Observations. *Langmuir* **2010**, *26*, 13650−13654.

(18) Nimmala, P. R.; Jupally, V. R.; Dass, A. Core Size Conversion: Route for Exclusive Synthesis of Au_{38} or Au_{40} Nanomolecules. *Langmuir* **2014**, *30*, 2490−2497.

(19) Jin, S. S.; Meng, X. M.; Jin, S.; Zhu, M. Z. High Yield Synthesis of Au_{25} Nanoclusters by Controlling the Reduction Process. *J. Nanosci. Nanotechnol.* **2013**, *13*, 1282−1285.

(20) Bertino, M. F.; Sun, Z. M.; Zhang, R.; Wang, L. S. Facile Syntheses of Monodisperse Ultrasmall Au Clusters. *J. Phys. Chem. B* **2006**, *110*, 21416−21418.

(21) Koegler, P.; Clayton, A.; Thissen, H.; Santos, G. N. C.; Kingshott, P. The Influence of Nanostructured Materials on Biointerfacial Interactions. *Adv. Drug Delivery Rev.* **2012**, *64*, 1820−1839.

(22) Kumar, A.; Huo, S. D.; Zhang, X.; Liu, J.; Tan, A.; Li, S. L.; Jin, S. B.; Xue, X. D.; Zhao, Y. Y.; Ji, T. J.; et al. Neuropilin-1-Targeted Gold Nanoparticles Enhance Therapeutic Efficacy of Platinum(IV) Drug for Prostate Cancer Treatment. *ACS Nano* **2014**, *8*, 4205−4220.

(23) Llevot, A.; Astruc, D. Applications of Vectorized Gold Nanoparticles to the Diagnosis and Therapy of Cancer. *Chem. Soc. Rev.* **2012**, *41*, 242−257.

(24) Ahmad, M. Z.; Akhter, S.; Rahman, Z.; Akhter, S.; Anwar, M.; Mallik, N.; Ahmad, F. J. Nanometric Gold in Cancer Nanotechnology: Current Status and Future Prospect. *J. Pharm. Pharmacol.* **2013**, *65*, 634−651.

(25) Tran, N. T.; Powell, D. R.; Dahl, L. F. Nanosized $Pd_{145}(CO)_x(PEt_3)_{30}$ Containing a Capped Three-Shell 145-Atom Metal-Core Geometry of Pseudo Icosahedral Symmetry. *Angew. Chem., Int. Ed.* **2000**, *39*, 4121−4125.

(26) Schaaff, T. G.; Shafigullin, M. N.; Khoury, J. T.; Vezmar, I.; Whetten, R. L. Properties of a Ubiquitous 29 kDa Au: Sr Cluster Compound. *J. Phys. Chem. B* **2001**, *105*, 8785−8796.

(27) Chaki, N. K.; Negishi, Y.; Tsunoyama, H.; Shichibu, Y.; Tsukuda, T. Ubiquitous 8 and 29 kDa Gold: Alkanethiolate Cluster Compounds: Mass-Spectrometric Determination of Molecular Formulas and Structural Implications. *J. Am. Chem. Soc.* **2008**, *130*, 8608−8610.

(28) Fields-Zinna, C. A.; Sardar, R.; Beasley, C. A.; Murray, R. W. Electrospray Ionization Mass Spectrometry of Intrinsically Cationized Nanoparticles, $[Au_{144/146}(SC_{11}H_{22}N(CH_2CH_3)_3{}^+)_x(S(CH_2)_5CH_3)_y]^{x+}$. *J. Am. Chem. Soc.* **2009**, *131*, 16266−16271.

(29) Qian, H. F.; Jin, R. C. Controlling Nanoparticles with Atomic Precision: The Case of $Au_{144}(SCH_2CH_2Ph)_{60}$. *Nano Lett.* **2009**, *9*, 4083−4087.

(30) Lopez-Acevedo, O.; Akola, J.; Whetten, R. L.; Grönbeck, H.; Häkkinen, H. Structure and Bonding in the Ubiquitous Icosahedral Metallic Gold Cluster $Au_{144}(SR)_{60}$. *J. Phys. Chem. C* **2009**, *113*, 5035−5038.

(31) Bahena, D.; Bhattarai, N.; Santiago, U.; Tlahuice, A.; Ponce, A.; Bach, S. B. H.; Yoon, B.; Whetten, R. L.; Landman, U.; Jose-Yacaman, M. STEM Electron Diffraction and High-Resolution Images Used in the Determination of the Crystal Structure of the $Au_{144}(SR)_{60}$ Cluster. *J. Phys. Chem. Lett.* **2013**, *4*, 975−981.

(32) Wong, O. A.; Heinecke, C. L.; Simone, A. R.; Whetten, R. L.; Ackerson, C. J. Ligand Symmetry-Equivalence on Thiolate Protected Gold Nanoclusters Determined by NMR Spectroscopy. *Nanoscale* **2012**, *4*, 4099−4102.

(33) Tlahuice-Flores, A.; Black, D. M.; Bach, S. B. H.; Jose-Yacaman, M.; Whetten, R. L. Structure & Bonding of the Gold-Subhalide Cluster I-$Au_{144}Cl_{60}[Z]$. *Phys. Chem. Chem. Phys.* **2013**, *15*, 19191−19195.

(34) Negishi, Y.; Sakamoto, C.; Ohyama, T.; Tsukuda, T. Synthesis and the Origin of the Stability of Thiolate-Protected Au_{130} and Au_{187} Clusters. *J. Phys. Chem. Lett.* **2012**, *3*, 1624−1628.

(35) Jupally, V. R.; Dass, A. Synthesis of $Au_{130}(SR)_{50}$ and $Au_{(130-x)}Ag_{(x)}(SR)_{50}$ Nanomolecules through Core Size Conversion of Larger Metal Clusters. *Phys. Chem. Chem. Phys.* **2014**, *16*, 10473−10479.

(36) Tlahuice-Flores, A.; Santiago, U.; Bahena, D.; Vinogradova, E.; Conroy, C. V.; Ahuja, T.; Bach, S. B. H.; Ponce, A.; Wang, G. L.; Jose-Yacaman, M.; et al. Structure of the Thiolated Au-130 Cluster. *J. Phys. Chem. A* **2013**, *117*, 10470−10476.

(37) Bencsath, F. A.; Field, F. H. Ion Retardation and Collision-Induced Dissociation in the Thermospray Ion Source. *Anal. Chem.* **1988**, *60*, 1323−1329.

(38) Hamdan, M.; Curcuruto, O. Collision-Induced Dissociation of Some Protonated Peptides with and without Mass Selection. *Rapid Commun. Mass Spectrom.* **1994**, *8*, 274−279.

(39) Bure, C.; Gobert, W.; Lelievre, D.; Delmas, A. In-Source Fragmentation of Peptide Aldehydes and Acetals: Influence of Peptide Length and Charge State. *J. Mass Spectrom.* **2001**, *36*, 1149−1155.

(40) Makowiecki, J.; Tolonen, A.; Uusitalo, J.; Jalonen, J. Cone Voltage and Collision Cell Collision-Induced Dissociation Study of Triphenylethylenes of Pharmaceutical Interest. *Rapid Commun. Mass Spectrom.* **2001**, *15*, 1506−1513.

(41) Weinmann, W.; Stoertzel, M.; Vogt, S.; Svoboda, M.; Schreiber, A. Tuning Compounds for Electrospray Ionization/In-Source Collision-Induced Dissociation and Mass Spectra Library Searching. *J. Mass Spectrom.* **2001**, *36*, 1013−1023.

(42) Sleno, L.; Volmer, D. A. Ion Activation Methods for Tandem Mass Spectrometry. *J. Mass Spectrom.* **2004**, *39*, 1091−1112.

(43) Lee, S. H.; Choi, D. W. Comparison between Source-Induced Dissociation and Collision-Induced Dissociation of Ampicillin, Chloramphenicol, Ciprofloxacin, and Oxytetracycline Via Mass Spectrometry. *Toxicol. Res.* **2013**, *29*, 107−114.

(44) Williams, J. D.; Flanagan, M.; Lopez, L.; Fischer, S.; Miller, L. A. Using Accurate Mass Electrospray Ionization-Time-of-Flight Mass Spectrometry with In-Source Collision-Induced Dissociation to Sequence Peptide Mixtures. *J. Chromatogr. A* **2003**, *1020*, 11−26.

(45) Sleno, L.; Volmer, D. A. Ion Activation Methods for Tandem Mass Spectrometry. *J. Mass Spectrom.* **2004**, *39*, 1091−1112.

(46) van Dongen, W. D.; van Wijk, J. I. T.; Green, B. N.; Heerma, W.; Haverkamp, J. Comparison between Collision Induced Dissociation of Electrosprayed Protonated Peptides in the Up-Front Source Region and in a Low-Energy Collision Cell. *Rapid Commun. Mass Spectrom.* **1999**, *13*, 1712−1716.

(47) Bure, C.; Lange, C. Comparison of Dissociation of Ions in an Electrospray Source, or a Collision Cell in Tandem Mass Spectrometry. *Curr. Org. Chem.* **2003**, *7*, 1613−1624.

(48) Wang, Z.; Wan, K. X.; Ramanathan, R.; Taylor, J. S.; Gross, M. L. Structure and Fragmentation Mechanisms of Isomeric T-Rich Oligodeoxynucleotides: A Comparison of Four Tandem Mass Spectrometric Methods. *J. Am. Soc. Mass Spectrom.* **1998**, *9*, 683−691.

(49) Hamouda, R.; Bertorelle, F.; Rayane, D.; Antoine, R.; Broyer, M.; Dugourd, P. Glutathione Capped Gold $Au_N(SG)_M$ Clusters Studied by Isotope-Resolved Mass Spectrometry. *Int. J. Mass Spectrom.* **2013**, *335*, 1−6.

(50) Tracy, J. B.; Crowe, M. C.; Parker, J. F.; Hampe, O.; Fields-Zinna, C. A.; Dass, A.; Murray, R. W. Electrospray Ionization Mass Spectrometry of Uniform and Mixed Monolayer Nanoparticles: $Au_{25}[S(CH_2)_2Ph]_{18}$ and $Au_{25}[S(CH_2)_2Ph]_{18-x}(SR)_x$. *J. Am. Chem. Soc.* **2007**, *129*, 16209−16215.

(51) Tracy, J. B.; Kalyuzhny, G.; Crowe, M. C.; Balasubramanian, R.; Choi, J. P.; Murray, R. W. Poly(Ethylene Glycol) Ligands for High-Resolution Nanoparticle Mass Spectrometry. *J. Am. Chem. Soc.* **2007**, *129*, 6706−+.

(52) Harkness, K. M.; Fenn, L. S.; Cliffel, D. E.; McLean, J. A. Surface Fragmentation of Complexes from Thiolate Protected Gold Nanoparticles by Ion Mobility-Mass Spectrometry. *Anal. Chem.* **2010**, *82*, 3061−3066.

(53) Harkness, K. M.; Hixson, B. C.; Fenn, L. S.; Turner, B. N.; Rape, A. C.; Simpson, C. A.; Huffman, B. J.; Okoli, T. C.; McLean, J. A.; Cliffel, D. E. A Structural Mass Spectrometry Strategy for the Relative Quantitation of Ligands on Mixed Monolayer-Protected Gold Nanoparticles. *Anal. Chem.* **2010**, *82*, 9268−9274.

(54) Angel, L. A.; Majors, L. T.; Dharmaratne, A. C.; Dass, A. Ion Mobility Mass Spectrometry of $Au_{25}(SCH_2CH_2Ph)_{18}$ Nanoclusters. *ACS Nano* **2010**, *4*, 4691−4700.

(55) Madsen, J. A.; Brodbelt, J. S. Comparison of Infrared Multiphoton Dissociation and Collision-Induced Dissociation of Supercharged Peptides in Ion Traps. *J. Am. Soc. Mass Spectrom.* **2009**, *20*, 349−358.

(56) Huang, T. Y.; Kharlamova, A.; Liu, J.; McLuckey, S. A. Ion Trap Collision-Induced Dissociation of Multiply Deprotonated RNA: C/Y-Ions Versus (a-B)/W-Ions. *J. Am. Soc. Mass Spectrom.* **2008**, *19*, 1832−1840.

(57) He, M.; Reid, G. E.; Shang, H.; Lee, G. U.; McLuckey, S. A. Dissociation of Multiple Protein Ion Charge States Following a Single Gas-Phase Purification and Concentration Procedure. *Anal. Chem.* **2002**, *74*, 4653−4661.